CuCrZr alloy obtained via electron-beam powder bed fusion: Microstructural insights and precipitation behaviour

Materials Characterization 218 (2024) 114559

Contents lists available at ScienceDirect

Materials Characterization

journal homepage: www.elsevier.com/locate/matchar

CuCrZr alloy obtained via electron-beam powder bed fusion: Microstructural insights and precipitation behaviour

Stefano Felicioni [a,*], Elisa Padovano [a,b], Federica Bondioli [a,b], Paolo Fino [a,b]

[a] Department of Applied Science and Technology, Politecnico di Torino, Corso Duca degli Abruzzi 24, 10129 Torino, Italy
[b] Consorzio Interuniversitario Nazionale per la Scienza e Tecnologia dei Materiali (INSTM), Via G. Giusti 9, 50121 Firenze, Italy

ARTICLE INFO

Keywords:
Additive manufacturing
Electron beam powder bed fusion
CuCrZr
C18150
CU-169
Phase transformation
Densification behaviour
Microstructure
Mechanical properties

ABSTRACT

An in-depth characterization of microstructure and mechanical properties of CuCrZr alloy processed by electron beam powder bed fusion (EB-PBF) additive manufacturing technology was performed with the aim to investigate the effect the thermal history of the material during the building process has on the properties of printed parts. Fully dense samples with a relative density up to 99.77 ± 0.04 % were successfully obtained in optimized conditions. The samples in the as-built condition exhibit an anisotropic microstructure dependent on the energetic input. An extensive microstructural transformation occurs alongside the precipitation and segregation of chromium-rich species, driven by the elevated thermal conditions during the deposition process. This unique thermal evolution can be properly investigated and exploited to eliminate the need for further post-processing heat treatments. To identify and quantify the precipitations within the microstructure, scanning and transmission electron microscopy together with electron backscattered diffraction were used.

1. Introduction

A growing interest in various industrial sectors has recently turned to the management and optimization of high heat flux applications such as rocketry and nuclear reactor components, which demand materials with high thermal conductivity to rapidly transfer heat through active or passive cooling mechanisms. For this purpose, copper has emerged as one of the most studied materials, boasting a thermal conductivity of approximately 400 W/mK along with excellent formability, electrical conductivity, and corrosion resistance properties [1].

In the selection of alloys for high-temperature applications, however, it is essential to consider also robust resistance to microstructural changes and effective mechanical reinforcement. In fact, many metals, including copper, suffer from a loss of mechanical stability and a decline in mechanical properties at elevated temperatures. Therefore, viable alternatives were studied including copper-chromium systems like CuCrZr, which offer improved mechanical stability even under high-temperature conditions [2]. CuCrZr is a promising precipitation hardenable (PH) alloy for thermal management applications thanks to the limited solubility of chromium and zirconium in copper which form strengthening intermetallic secondary phases. In particular, in the ternary CuCrZr system, the presence of coherent precipitates, such as Cr or $Cu_x Zr_y$ compounds (e.g. $Cu_4 Zr$ and $Cu_5 Zr$), predominates, modifying the microstructures and enhancing the physical properties of the system by introducing strengthening species that are significantly stronger than the Cu-matrix and resistant to particle shear, thereby making Orowan strengthening the primary mechanism for dispersoid reinforcement [3,4].

The achievement of satisfactory functional and mechanical properties of the material, in most cases require an appropriate post-built heat treatment, between solution aging heat treatment (SAHT) or direct aging heat treatment (DAHT). The main objective of these treatments is to get a supersaturated solid solution leading to the formation of ultrafine homogeneous precipitation of the aforementioned Cr-rich species [5].

Regarding the processes of these alloys, high values of area-to-volume ratio, necessary for thermal and heat transfer applications, and the increasing capabilities in fabricating complex structures, triggered an increasing interest in the design of high-performance components by Additive manufacturing (AM) [6]. In addition to the design freedom, AM offers significant advantages coming from the rapid solidification and cooling processes it facilitates. In fact, in PH alloys, the quantity of solid secondary-phase precipitation is directly related to the concentration of solute in supersaturation, rather than solely to the

* Corresponding author.
E-mail address: stefano.felicioni@polito.it (S. Felicioni).

https://doi.org/10.1016/j.matchar.2024.114559
Received 4 August 2024; Received in revised form 25 October 2024; Accepted 13 November 2024
Available online 19 November 2024

solubility at the aging temperature [2,7].

Despite the widespread use of laser-based additive manufacturing technologies, their use for the processing of copper remains challenging. In techniques such as laser powder bed fusion (L-PBF), in fact, the effectiveness of the process greatly depends on the interaction between the laser and the metal powder. Pure copper exhibits high reflectivity at near-infrared (IR) laser wavelengths commonly employed in many commercial L-PBF systems [4]. Therefore, it is crucial to carefully adjust the process parameters to achieve satisfactory results [8]. Notable examples in literature involving the use of high-power IR lasers include the process development studies conducted by Yang et al. [9] and Salvan et al. [10].

In this context, the adoption of the electron beam powder bed fusion (EB-PBF) is a promising alternative due to the distinctive advantages offered by this technology. In fact, the use to an electron beam instead of a laser source makes EB-PBF unaffected by optical reflectivity of the materials; furthermore, the additional advantage of preventing oxidation in a vacuum environment makes this process very promising for the processing of pure copper and its alloys. Finally, EB-PBF can be classified as a hot process, hence a proper tuning of process parameters allows a specific thermal target to be reached, which can be maintained during the entire scanning process.

Surprisingly, the application of EB-PBF in the additive manufacturing (AM) of copper and its alloys has not been widely demonstrated. Ramirez et al. [11] have successfully manufactured both cellular and solid copper structures containing 0.2 % oxygen, a composition that thanks to the heated chamber of EB-PBF results in remarkable precipitation hardening. Gushblauer et al. [12] achieved an almost complete densification of pure copper samples by EB-PBF and conducted an extensive investigation of their mechanical properties, obtaining results comparable to those obtained through traditional manufacturing methods. Wolf et al. [13], successfully achieved Cu—Al components via EB-PBF reporting how the process is able to improve the mechanical properties of this bronze with the proper tuning of the parameters. Similarly, Yu et al. described how the employment of EB-PBF technology is effective in the development of Cu—Al system reporting a detailed analysis of complex precipitation mechanism involved in the process. However, to the knowledge of the authors, only Ordàs et al. [5,14] showed that high density CuCrZr samples obtained by EB-PBF exhibit interesting hardness values already in *as-built* condition.

In order to better investigate these findings, this paper aims to present a comprehensive study of EB-PBF CuCrZr samples, attempting to cover the inadequate amount of literature addressing the relationship between microstructure and precipitation behaviour as a function of the thermal conditions and processing parameters encountered during the deposition process, formally establishing the basis for the selection of most viable post processing condition [9]. The results of this investigation can serve as a reference for the exploration of precipitation-hardening copper alloys by EB-PBF offering valuable insights into the utilization and structural planning of rocket engine thrusters and fusion reactor heat sinks.

2. Materials and methods

2.1. Materials

EB-PBF samples were built by using an argon atomized powder supplied by Praxair (Praxair Surface Technology ltd., WA, USA) in a spherical range 15-45μm. The chemical composition of the feedstock, according to the conformity report, is reported in Table 1. The alloying elements content is in compliance with the EN10204:2004-type 3.1 standard [15]; moreover, the composition matches the ITER (international thermonuclear experimental reactor) grade specification.

Table 1
Powder chemical report. All data are expressed as wt%.

Chemistry	Test method	Min	Max	Result
Copper	Difference	98.00	–	98.86
Chromium	ICP	0.5	1.50	0.84
Zirconium	ICP-MS	0.05	0.20	0.06

2.2. Experimental

All specimens were built using a Freemelt-One (Freemelt AB, Sweden) EB-PBF system. This equipment is outfitted with an electron beam gun capable of generating a beam within the energy spectrum from 1 to 60 keV, with a maximum power output of 6 kW. The vacuum system enables material processing under high vacuum conditions at pressures as low as 10^{-6} mbar. The selection of process parameters followed a trial-and-error procedure based on a study conducted by Gushblauer et al. on pure copper [16]. Massive cubes with a size of 12 × 12 × 12 mm^3 were built on a circular steel platform in AISI 304 with a diameter of 100 mm. During the melting sequence, process parameters optimization was carried out with a melting power of 720 W, varying the scan speed from 300 to 1100 mm/s, and the hatch distance from 15 to 20 μm; conversely, the layer thickness was fixed to 50 μm and an interlayer rotation of 90° was adopted. The preheating and the post cooling sequences were optimized to guarantee a thermal target of the powder bed in the optimal aging temperature of the material (610 °C).

The detailed process parameters investigated during two experimental sessions are reported in Table 2, along with the values of volume energy density (VED) [J/mm^3] defined as follows:

$$VED = \frac{p}{vhl} \tag{1}$$

where p is the beam power, v the scanning speed, h and l the line offset and layer thickness, respectively.

As a preliminary investigation, the first session was designed with a wide VED range to study the densification behaviour. The second session involved a more precise refinement to identify the optimal process window.

2.3. Material characterization

The built cubes were cut in planes both parallel and perpendicular to the building direction (identified as XY and XZ, respectively), and the resulting cross sections underwent a multi-step polishing process firstly including the use of fine abrasive papers (1200–2400 grit), followed by diamond (6–1 μm) and colloidal silica suspensions.

Table 2
Samples process parameters using 720 W as beam power, 50 μm as layer thickness and 90° as interlayer rotation.

Deposition number	Sample code	Scan speed [mm/s]	Line offset [mm]	VED [J/mm^3]
Job 1	S1_1	300	0.20	240,0
	S1_2	400	0.20	180,0
	S1_3	500	0.20	144,0
	S1_4	600	0.20	120,0
	S1_5	700	0.20	102,9
	S1_6	800	0.20	90,0
	S1_7	900	0.20	80,0
	S1_8	1000	0.20	72,0
	S1_9	1100	0.20	65,5
Job 2	S2_1	450	0.15	213,3
	S2_2	500	0.15	192,0
	S2_3	550	0.15	174,5
	S2_4	600	0.15	160,0
	S2_5	650	0.15	147,7
	S2_6	700	0.15	137,1
	S2_7	750	0.15	128,0
	S2_8	800	0.15	120,0
	S2_9	850	0.15	112,9

To investigate the degree of densification through image analysis, half of each sample was examined using the optical microscope (OM) Leica DMI 5000 M (Leica Microsystems GmbH, Germany). For each sample, 30 images were collected at a magnification of 50×, analysing different heights from bottom to top to conduct a statistical survey of porosity distribution using ImageJ software. The remaining half of each cube were employed for density determination using the helium pycnometer Anton Paar ULTRAPYC 5000 (Anton Paar GmbH, Austria), with fresh powder skeletal density serving as reference.

For microstructure examination, etching using a mixed solution of 1.5 g $FeCl_3$, 10 ml HCl, and 30 ml distilled H_2O for 10 s was performed to highlight grain morphology while, to reveal melt pools, electro-etching using a voltage of 3 V with a mixture of 10 ml NH_4OH, 10 ml distilled H_2O, and 20 ml H_2O_2 was used for 45 s.

Morphology and microstructure of the built samples were evaluated also by scanning electron microscopy (SEM). A TESCAN S9000G (Tescan Group a.s., Czech Republic) field emission gun equipped with energy dispersion spectroscopy (EDS) and electron backscattered diffraction (EBSD) detectors was used for this purpose. EBSD was employed for the assessment of average grain size and median misorientation angle. The Aztec Crystal (Oxford Instruments plc., UK) software was adopted for data processing. Grain boundaries were defined based on a misorientation angle exceeding 15°, while sub grain boundaries were delineated by misorientation angles below 15°. Grain size was determined as the equivalent diameter of a circle with the same surface area as the observed grains, with the average grain size calculated based on weighted surface area. In addition, a Kernel Average Misorientation map (KAM) analysis was collected to gauge local misorientation, ranging from 0.5° to 5°, relative to adjacent pixels. This angle (θ [rad]) was used to estimate dislocation density (ρ_0) using the following equation [17]:

$$\rho_0 = \frac{2\sqrt{3}\theta}{3bs} \tag{2}$$

where b[m] is the Burgers vector (assumed 0.256 nm for a Cu matrix [18]) and s[m] the step size employed in the EBSD analysis (0,375 μm).

For further microstructural characterization, a Philips CM20 (Koninklijke Philips N.V., Netherlands) transmission electron microscope (TEM), operated at 200 keV and equipped with double tilt specimen holder cooled with liquid nitrogen, was used. TEM thin foils were mechanically prepared by polishing down to 0.25 μm, punching, dimpling on both sides and then finally thinned to electron transparency using a precise ion polishing device PIPS GATAN 691 (Gatan Inc., CA USA), working at 12 *V*. The Ar^+ twin beam was set as to progressively decreasing incident angles from 8° to 4° respect to the thin disc surface.

Statistic evaluations of mean size, distribution, and volume fraction of the quasi-spherical Cu—Cr particles were carried out by orienting the foil normal to the [110] direction. Foil thickness, t_{TEM}, was measured by converged electron beam diffraction (CEBD). This was performed by analysing the corresponding diffracted beam intensity variation under dual beam conditions. Thence, linear interpolation of data points in a $s^2/n^2_{fringes}$ vs. $n^{-2}_{fringes}$ plot, where *S* is the fringes spacing, and $n_{fringes}$ the number of counted fringes, was used to determine t_{TEM}.

Particle size, *d*, was measured by stereographic methods according to EN-112 [19], using a Leica Image pro-plus image analysis software. Particle volume fraction, f_V, was determined by Woodhead method in which the volume number fraction is determined by $N_V = N_A/d$. For each size group, $N_{A(i)} = \frac{n_i}{A/M^2}$ represents the thin foil area fraction along (110) crystallographic planes, n_i are the number of particles in specific size groups, and *A* is the area from which particle sizes are measured and counted at magnification *M*. Thence:

$$N_{V(i)} = \frac{N_{A(i)}}{t_{TEM} + \left(i - \frac{1}{2}\right)\Delta} \tag{3}$$

being t_{TEM} the thin foil thickness measured in the acquisition area, and $\left(i - \frac{1}{2}\right)D$ is the mean diameter in the size group (i) where Δ represents the size increment between groups. Using this stereological approach, the Cr-rich quasi-spherical phase particle volume fraction was calculated as follows:

$$f_V = \frac{\pi}{6}\Delta^3 \sum_i \left[N_{V(i)} \left(i - \frac{1}{2}\right)^3 \right] \tag{4}$$

More than 500 particles were measured out of several TEM areas for the two samples selected after the parameter optimization process.

To check the degree of precipitation of *as-built* EB-PBF specimens, different scanning calorimeter tests (DSC) were carried out using the TGA-DSC Setaram 92/16.18 (Setaram Instrumentation co. France) in a temperature range from room temperature to 1200 °C with a heating rate of 10 °C/s.

Finally, an estimation of the mechanical performances of the material was made by means of Vickers micro-hardness tests using a Leica VMHT apparatus with a 100gf load applied for 15 s, following the guidelines outlined in ASTM E384 [20].

3. Results and discussion

3.1. Densification behaviour

Fig. 1 illustrates, as a function of VED, the trend of relative density of the built samples extracted from the pycnometer measurements. Specifically, the VED range under investigation can be divided into four areas from ((a) to (d)), exhibiting specific characteristics and typical defects, as reported in the corresponding optical micrographs of the XZ cross section.

Inadequate energy input (areas (a) and (b) in the scatter plot) leads to insufficient bonding among tracks and layers, resulting in defects (Fig. 1 (a) and (b)) such as significant lack of fusion and grain boundary cracks. The latter, which characterize the samples in area (b) such as the one reported for sample S2_6, are a well-documented issue in copper processed through EB-PBF, as highlighted in the review by Sharabian et al. [21]. The residual oxygen content is primarily responsible for crack formation along the grain boundaries due to the embrittlement effects of the Cu2O phase in Ductile Dip Cracking (DDC).

Material shrinkage during solidification leads to grain boundary sliding or shearing, similar to creep. This mechanism results in a smooth, wavy crack surface and finely dispersed Cu_2O particles within the copper matrix, which increases brittleness. The exact role of oxides on the fracture surface remains unclear. If the oxides do not anchor the grain boundaries, the crack can propagate.

Increasing the scanning speed, significantly reduces the molten volume in a stationary regime [22], thereby decreasing the solidification time.

Under the chamber's vacuum conditions (10^{-4} bar), the stability temperature range for Cu_2O shifts to lower temperatures [21]. Consequently, under optimal deposition conditions, the solidification time is long enough for the oxygen to react and form more stable phases with other alloying elements, as will be discussed in subsequent sections. Conversely, increasing the scanning speed, decrease the molten pool residence time, where the temperature quickly drops to the chamber temperature, intersecting the stability temperature of Cu_2O. This leads to Cu_2O segregation at the grain boundaries, which are the outermost region during solidification.

Although these cracks may not impact overall densification, as observed in samples S2_6 and S2_8, they can become significant in terms of tensile behaviour, particularly considering the deeply textured microstructure, that distinguish all the analysed samples as explored in greater detail in the following sections.

Conversely, an excess of energy input (area (d) in the graph) can

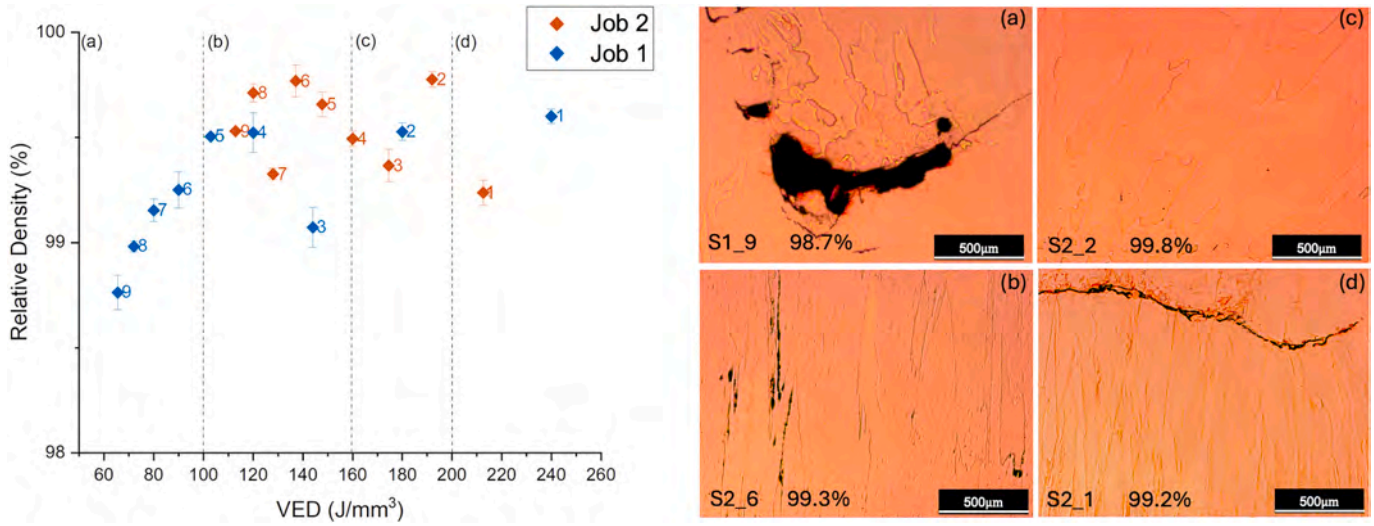

Fig. 1. Relative density as a function of VED (J/mm^3) and OM images reporting representative cross section parallels to the building direction of samples S1_9 (a), S2_6 (b), S2_2 (c) and S2_1(d).

induce the formation of horizontal cracks (Fig. 1(d)); this defect can be attributed to intense thermal stresses in the melt pool induced by significant heat transfer towards the substrate, which is the preferred direction of heat flow propagation. Notably, most of the samples within the region (c) in Fig. 1, shows relative density values around 99.5 %. Fig. 1(c) shows the optical micrograph of sample S2_2, as an example of near full dense obtained sample. Its residual porosity (≈0,2 %) appears as highly spherical with dimensions of few microns; this suggests its origin as residual gases coming from the powder itself [23].

It is worth noting that different combinations of process parameters, and consequently different VED values, can produce highly dense samples. Based on this finding, an in-depth characterization of two samples almost free of defect, from the previously mentioned region (c), was performed to investigate potential microstructural differences that could result in varying material properties. In this context, two specific combinations of process parameters which lead a densification of around 99.5 %, were selected for further detailed investigation and comparison: p = 720 W, v = 500 mm/s, l = 0.15 mm, h = 0.05 mm for sample 2_2, and p = 720 W, v = 550 mm/s, l = 0.15 mm, h = 0.05 mm for sample 2_3.

3.2. Optimized sample characterization

Fig. 2 shows the optical micrographs of chemical etched cross section of sample S2_3, chosen as representative, collected at the interface with the building platform (Fig. 2(a)) and far from the substrate (Fig. 2(b)), respectively. The sample microstructure evidences the presence of columnar grains that are aligned with the building direction. A similar low magnification microstructure can be observed for both the investigated specimens; the observed columnar grains originate from the starter plate through epitaxial growth over multiple fabricated layers.

This microstructure is characteristic of samples produced by EB-PBF process, where heat is transported through the solid material, and grain nucleation is suppressed due to the steep temperature gradient. This condition makes the electron beam a heat source with unique properties, as it did not induce the columnar-to equiaxed transition which is generally observed in materials produced by AM technologies. The spatial and temporal variation in energy density caused by the raster scanning of electron beam strongly influences the thermal gradient (G) as well as the solidification and cooling rate. This results in an elongated columnar grain structure with sinuous growth for the 90° interlayer rotation [24–26]. In fact, among the AM processes, the scanning strategy in EB-PBF is the most influential parameters for controlling the thermal transient which drastically influences the values of the temperature

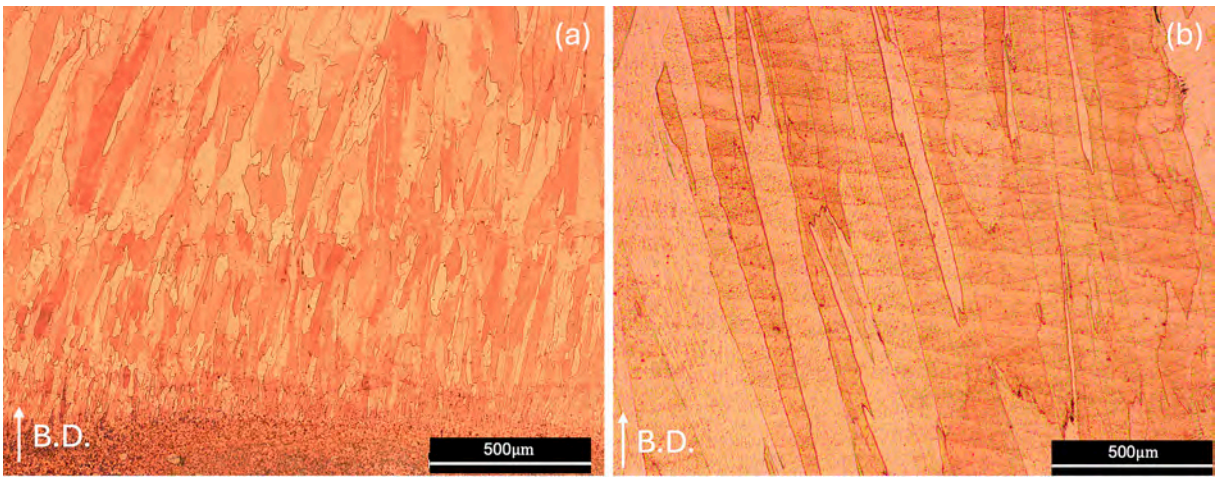

Fig. 2. OM micrographs in the direction parallels to the building direction (B.D.) of sample S2_3 at (a) the substrate interaction and (b) at the samples core.

gradient (G) and the travel speed of the solid/liquid interface (R) of the melt pool, thereby determining the microstructural evolution [27]. The choice of the 90° interlayer rotation was based on the symmetric geometry of the build samples, allowing the optimal homogenization of the supplied energy since it make possible the scanning of each layer in equal length lines.

A comparison between Fig. 2(a) and (b) evidenced that the grain size varies along the building direction. This behaviour can be explained considering that 304 SS substrate, even if preheated, behaves like a heat sink at the initial stages of the EB-PBF process; moreover, the caking effect of the powder bed impedes heat dissipation in the direction perpendicular to the build layers. As a result, very small grains are observed at the interface up to a height of around 2 mm from the substrate suggesting the necessity to support adoption to homogenise the microstructure. Directional solidification drives grain growth in the [100] direction, a condition that is very common in EB-PBF processes. Thomas et al. [22] extensively discussed the texture formation tendency in pure copper, while Helmer et al. [25] observed the same phenomenon in Ni-based superalloys. Grains that do not solidify in the [100] orientation tend to lag, providing an opportunity for neighbouring grains with the correct orientation to outgrow them.

To better understand the texture evolution, EBSD analysis were performed, which main results are reported in Fig. 3. Focusing the attention on the IPF maps (Fig. 3(a-d)) in both the characteristic cross sections, the preferred growth direction become more than evident for both the samples S2_2 and S2_3. Additionally, the pole figures of Fig. 3 (e-f) coming from the XZ sections, displays the orientation distribution of the (100) and (111) planes confirming the preferential orientation parallel to the building direction. The pronounced (111) texture also suggest a propensity of the material for slip, being this plane oriented diagonally in the FCC unitary cell, contributing positively to the ductility.

As the distance from the steel substrate increases, thermal stability is achieved, resulting in a noticeable increase in grain size. Table 3 compares the results obtained using the intercept method on the XZ micrographs, following ASTM E112 [19], with the average grain size measured by EBSD on the XY plane. Both parallel and perpendicular measurements to the building direction were taken at the mid-height of each sample. The results obtained with the two methods agree and underline a marked difference in grain size between the two experimental conditions, likely related to the initiation of recrystallization in the sample S2_3. This observation underscores how even slight variations in energy input can lead to substantial microstructural changes in directional solidification processes like this.

The recrystallization phenomenon is further evidenced by the significant discrepancy in the number of dislocation boundaries or LAGBs (misorientation angle lower than 10°) of the IPF mapping, and in the local misorientation analysis of the KAM maps reported in Fig. 3(g-h). The latter, from which the dislocation density was measured, shows a homogeneous local distortion distribution for both experimental conditions, across the entire grain section. Moreover, it is noteworthy that the KAM angle is strongly related to the grain size, minimizing in the smaller grains of the samples S2_2 and attaining much lower values in sample S2_3.

During recrystallization, new strain-free grains nucleate and grow, consuming the deformed, high-dislocation-density ones. This indicates that recrystallization developed more with higher scanning speed, involving in the reduction of the overall dislocation density within the material.

The optical micrographs of Fig. 4(a-b) resultant from the electro chemical etching on sample S2_2, chosen as representative of both samples, underline the melt pools shapes and are helpful to understand the morphological difference of the material inside the grains. The interaction between the high-power electron beam and the copper alloy results in the formation of melt pool with an elliptical shape and a microstructure which varies along the radial direction. The typical dimensions of the meltpools are reported in Fig. 4(b). Without remelting effects, the meltpool penetration depth is ~180 μm meaning that the remelting involves a volume of 3 times higher with respect to that of the deposited layer. In particular, the meltpool diameter and the layer thickness are coherent with the electron beam spot and the deposited powder layer being on average ~ 215 μm and ~ 65 μm respectively. The meltpool borders are evidenced by dark, line-like features. These features emerge due to the morphological evolution resulting from the complex solidification process and represent the transition lines between two different morphologies. To support these statements low magnification scanning electron microscopy is reported in Fig. 4(c).

As clearly visible in the reported onsets, along the solidification border there is the suppression of the secondary dendrite arms during the ongoing solidification. This phenomenon is due to the rapid change in solidification conditions, where the reduction in constitutional undercooling ahead of the solidification front leads to a transition from dendritic to cellular morphology. In fact, in the initial stages of the solidification, the travel speed of the solid/liquid interface (R) is low while the temperature gradient (G) is very high [20,24]; as a consequence, high G/R values lead to the formation of the columnar-dendritic microstructure [28]. As the solidification progresses, R increases and G decreases; in fact, the uniformly heated powder bed acts as a heat sink and provides a uniform high cooling rate (G × R) that results in the formation of the cellular structures without secondary arms.

The previously discussed dendritic evolution becomes more evident in Fig. 5 depicting the microstructure of the CuCrZr S2_2 sample obtained at increasing magnifications, ranging from lower (a) to higher (c) ones. It focuses on the previously discussed epitaxial growth evidencing the cellular sub-structure within the columnar grains, where rounded shape precipitates can be observed (Fig. 5(b) and (c)). Due to the limited size of precipitates the EDS spot analysis is not useful to understand the composition, it however registered an enrichment in Zr that is coherent with the characteristic precipitation of this alloy. At the optimized building temperature (610 °C), in fact, a precipitation of Zr-rich particles is expected to be obtained into the copper matrix. According to the literature, in fact, this alloy exhibits two distinct precipitation temperature ranges: one between 155 and 250 °C in which Zr start to precipitate and another one between 400 and 600 °C where also Cr is involved [29–31] with a significant enhancement of sample tensile properties.

To assess the extent of precipitation induced by the thermal evolution during the EB-PBF hot process, DSC tests were performed for the selected S2_2 and S2_3 samples. The experimental data are reported in Fig. 7 confirming a high degree of precipitation occurring during the process, as only a very low-intensity exothermic peak was observed within the temperature range from 400 to 600 °C (Fig. 6).

3.3. Precipitation behaviour

Higher magnification microscopy made possible to put in evidence the differences in the precipitation behaviour among the studied processing conditions. Fig. 7 reports the high-resolution in-lens FESEM micrographs of both samples, revealing the existence of two distinct type of precipitation morphologies that essentially differ in size: clusters measuring hundreds of nanometres (Fig. 7(a-b)), and isolated, round particles with average dimension of tens of nanometres (Fig. 7(d-e)).

The presence of a significant number of precipitates was anticipated by SEM analysis and confirmed by DSC behaviour. This outcome was something expected; the EB-PBF process has a thermal history that falls between that of laser powder bed fusion and traditional manufacturing methods. In laser-based additive processes, the rapid solidification of the molten pool typically results in almost complete retention of elements in solid solution. In contrast, traditional manufacturing methods, such as wrought and cast processes, are known from the literature to involve in the precipitation of large Cr-based particles exhibiting resistance also to solution annealing [32–34]; EB-PBF shows an intermediate thermal evolution because it combines the rapid solidification due to localized

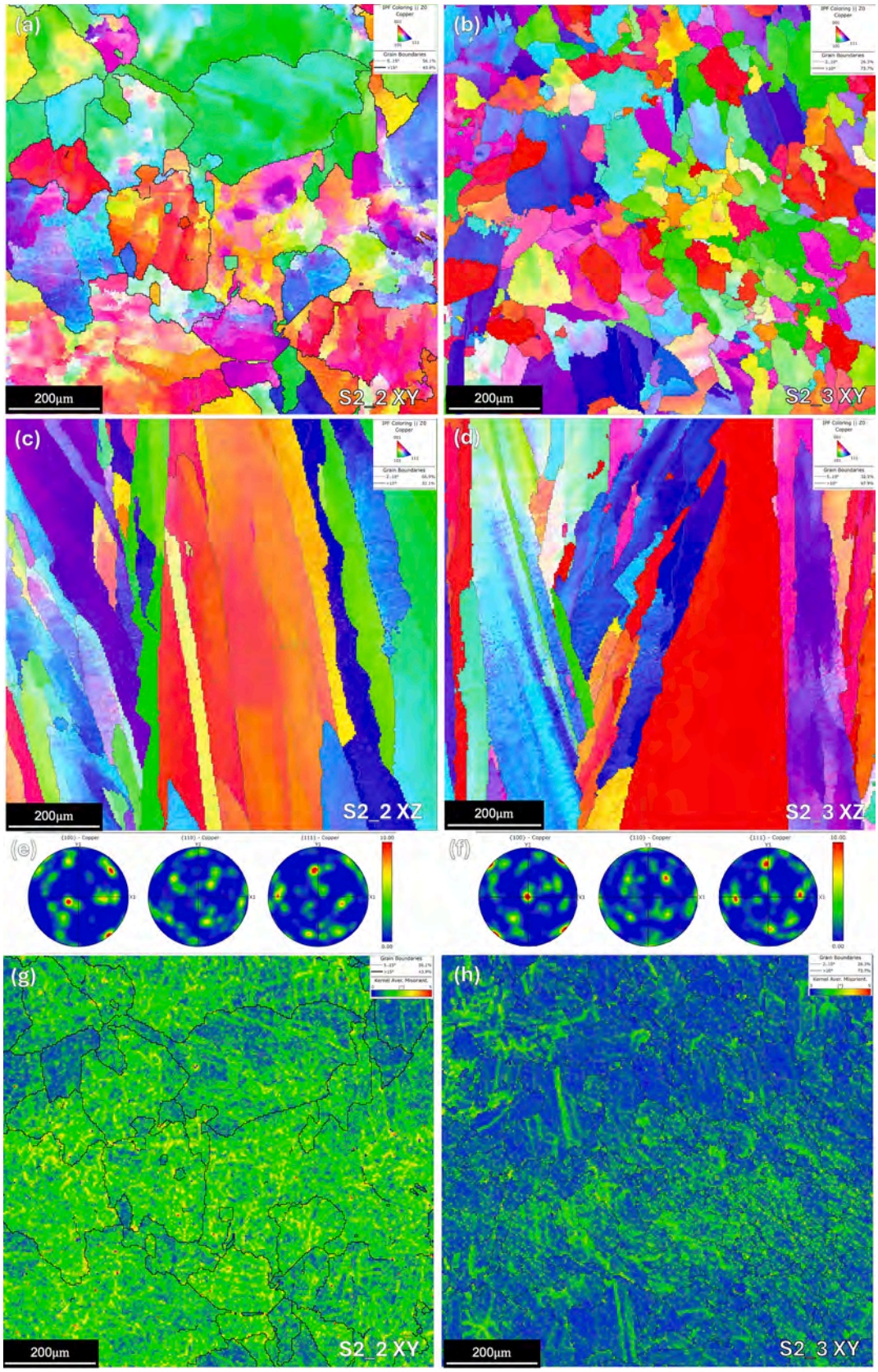

Fig. 3. EBSD of the CuCrZr samples a), b) EBSD IPF maps and grain boundaries XY plane parallel to the building platform; c), d) EBSD IPF maps and grain boundaries XZ plane parallel to the growth direction; e), f) pole figures of the samples in the XZ plane; g), h) KAM average misorientation maps XY plane.

Table 3
Average grain size of the different CuCrZr samples, KAM median misorientation angle θ and average dislocation density ρ0 according to Eq. (2).

	N° of grains counted (EBSD)	Avg. grain size ASTM E112 XZ [μm]	Avg. grain size EBSD XY [μm]	KAM Θ [°]	ρ_0 [m^{-2}]
S2_2	54,0	273,5 ± 13,8	274,2 ± 43,1	1,65 ± 0,6	3,71 × 10^{14}
S2_3	258,0	44,89 ± 6,1	53,1 ± 36,2	0,95 ± 0,4	2,13 × 10^{14}

melting characteristic of laser techniques with the caking effect.

The higher level of magnification revealed distinct differences between the two experimental conditions. The high-energy input conditions used for the fabrication of sample S2_2 (Fig. 7(a-c)) results in a significantly higher clustering tendency, suggesting enhanced nucleation and growth rates. Conversely, the condition for S2_3 (Fig. 7(d-f)) leads to the formation of smaller and more uniformly distributed precipitates, indicative of a more controlled nucleation process. In the high-energy scenario, clusters are distributed without a specific pattern; on the contrary, in sample S2_3, the precipitates tend to form along the sub-grain boundaries in the non-recrystallized regions.

TEM was employed to further study the nanoprecipitation. Fig. 8 show representative micrographs at different magnification of the S2_2 (Fig. 8(a-c)) and S2_3 (Fig. 8(d-f)) experimental condition, respectively. In both the S2_2 and S2_3 experimental conditions, almost spherical particles were mainly detected; however, some more geometrically structured (diamond-like) particles were also observed having the same size of the spherical particles. Selected area electron diffraction pattern (SAEDP) recorded at the diamond-like particles revealed that these are oxides, which SAEDP rings were consistent to Cr_2O_3 phase (Fig. 9). The same oxide identification is also reported and confirmed by Zhang et al. in the laser powder bed fusion of the same material [35].

This oxidation, which occurs during the additive process even under vacuum conditions, is primarily due to the presence of Cr. This element, available in solid solution within the alloy matrix, can react even with the small amounts of oxygen resulting from the thermal degradation of unavoidable residual copper oxides from the powder in the building chamber. Additionally, chromium oxides are much more stable than copper ones at low temperatures making difficult the dissolution by diffusion.

These oxides were invariably observed in both the S2_2 and S2_3 samples, with a slightly higher number fraction in S2_2 compared to S2_3 condition.

As per the quasi-spherical particles, especially in the S2_2 experimental condition, these often show coherent and semi-coherent contrast with the matrix typical of Guinier-Preston Zones (GPZ). The GPZs have a face-cantered cubic (fcc) crystallographic structure with a lattice parameter a = 0.367 nm [36]. In most cases, in the immediate vicinity of the GPZ, the spherical particles dissolve into Cr-rich and Zr-rich matrix zones. Fig. 10 illustrates a representative example of this feature observed in the S2_2 condition, along with the corresponding

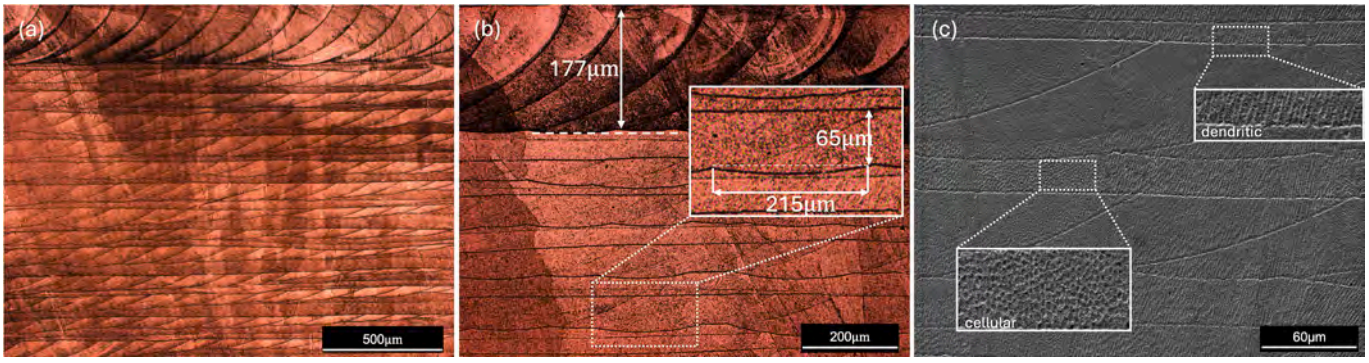

Fig. 4. OM and secondary electrons SEM images of sample S2_2 showing: (a) representative layered microstructure next to the top surface in the cross section along the building direction (XZ); (b) relative meltpool geometrical features; (c) microstructure morphology inside the meltpool: columnar dendritic at the border, cellular at the center.

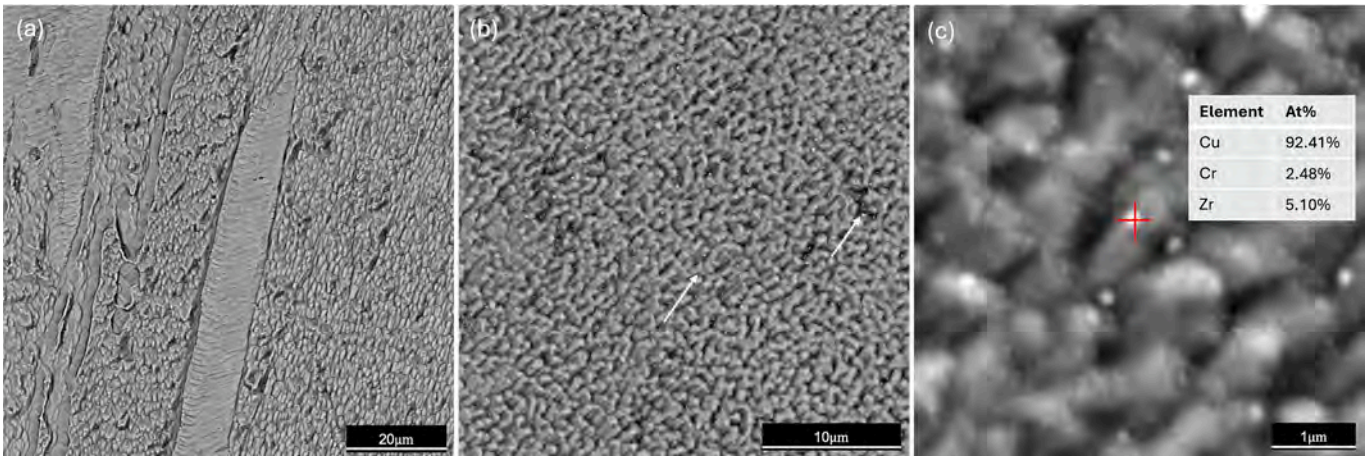

Fig. 5. Low magnification backscattered SEM images of sample S2_2 along the XZ cross section, chosen as representative, reporting: (a) epitaxial growth of primary dendrite arms inside the columnar grains; (b)-(c), Two different magnifications of the rounded shaped precipitates detected in the inter-dendritic regions (white arrows) which composition by EDS spot analysis is reported in onset table.

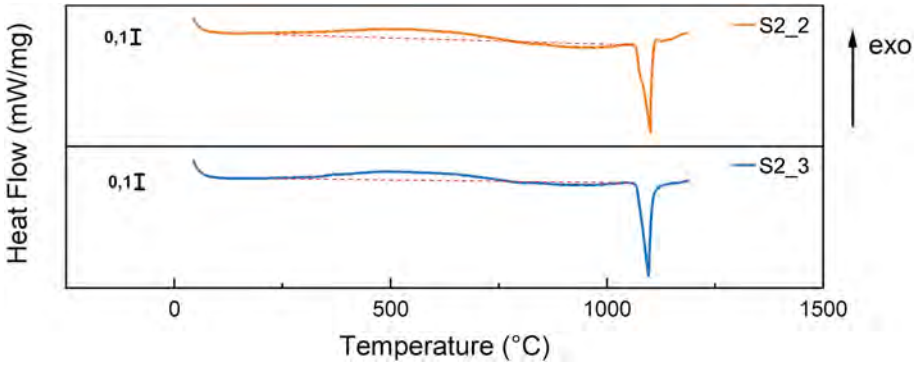

Fig. 6. DSC plots of the EB-PBF samples S2_2 and S2_3 in as-built condition.

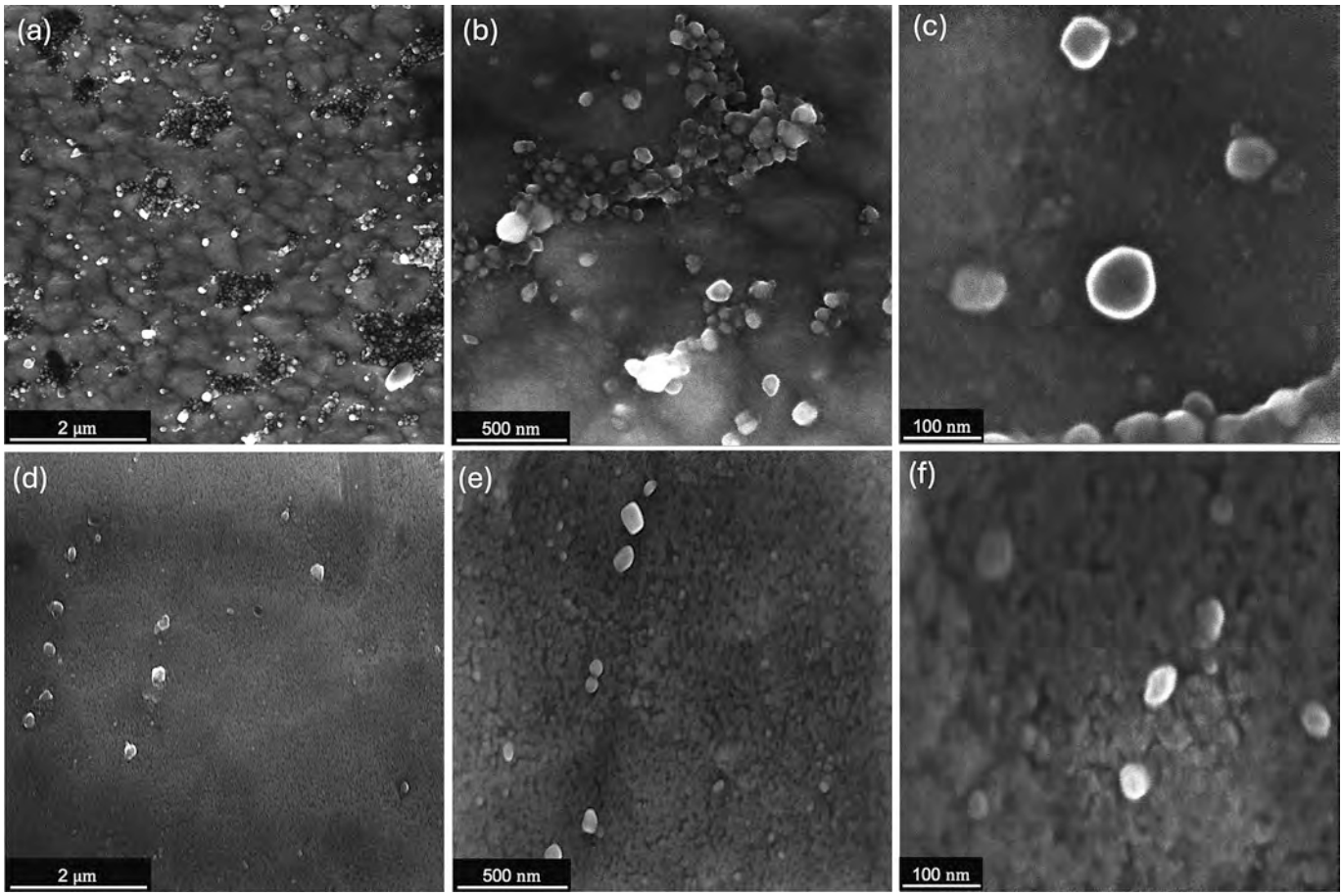

Fig. 7. In lens high resolution FESEM micrographs at different magnifications showing the morphology and precipitate distribution in the copper matrix for the EB-PBF CuCrZr samples under investigation S2_2 (a,b,c) and S2_3 (d,e,f).

SAEDP.

The SAEDP analysis revealed that the nanometric Cr-rich phase particles possess a body-cantered cubic (bcc) crystallographic structure. As depicted in Fig. 8(c) and (f) the reciprocal crystallographic relationship between the Cr-rich phase and the Cu matrix is characterized by (110) Cr-rich || (111) Cu-matrix and (100) Cr-rich || (110) Cu-matrix.

The coherency crystallography between the quasi-spherical Cr-rich nanometric particles and the Cu-matrix is on the (110) direction. The GPZ, other than the coherency with the matrix along the (110) direction, also shows Moiré fringes aligned along the (111) Cu-matrix orientation. This crystallographic coordination between the Cr-rich phase and the Cu-matrix and the corresponding atomic mismatch, δ, was measured by applying the following relationship:

$$\delta = \frac{|2(d_1 - d_2)|}{(d_1 + d_2)} \tag{5}$$

where d1 and d2 are the crystal plane spacing between the Cu-matrix and the Cr-rich phase, respectively. Thence, according to Fig. 11, where the two quantities were estimated as $d_1 = 1.2nm$ and $d_2 = 1.1nm$. respectively, it resulted a mismatch $d = 0.1$, value in quite good agreement with other previously reported values obtained in a similar alloy [37–39].

According to the results reported in the review paper by Tang et al. [40], the possible stoichiometry of the detected quasi-spherical Zr-rich

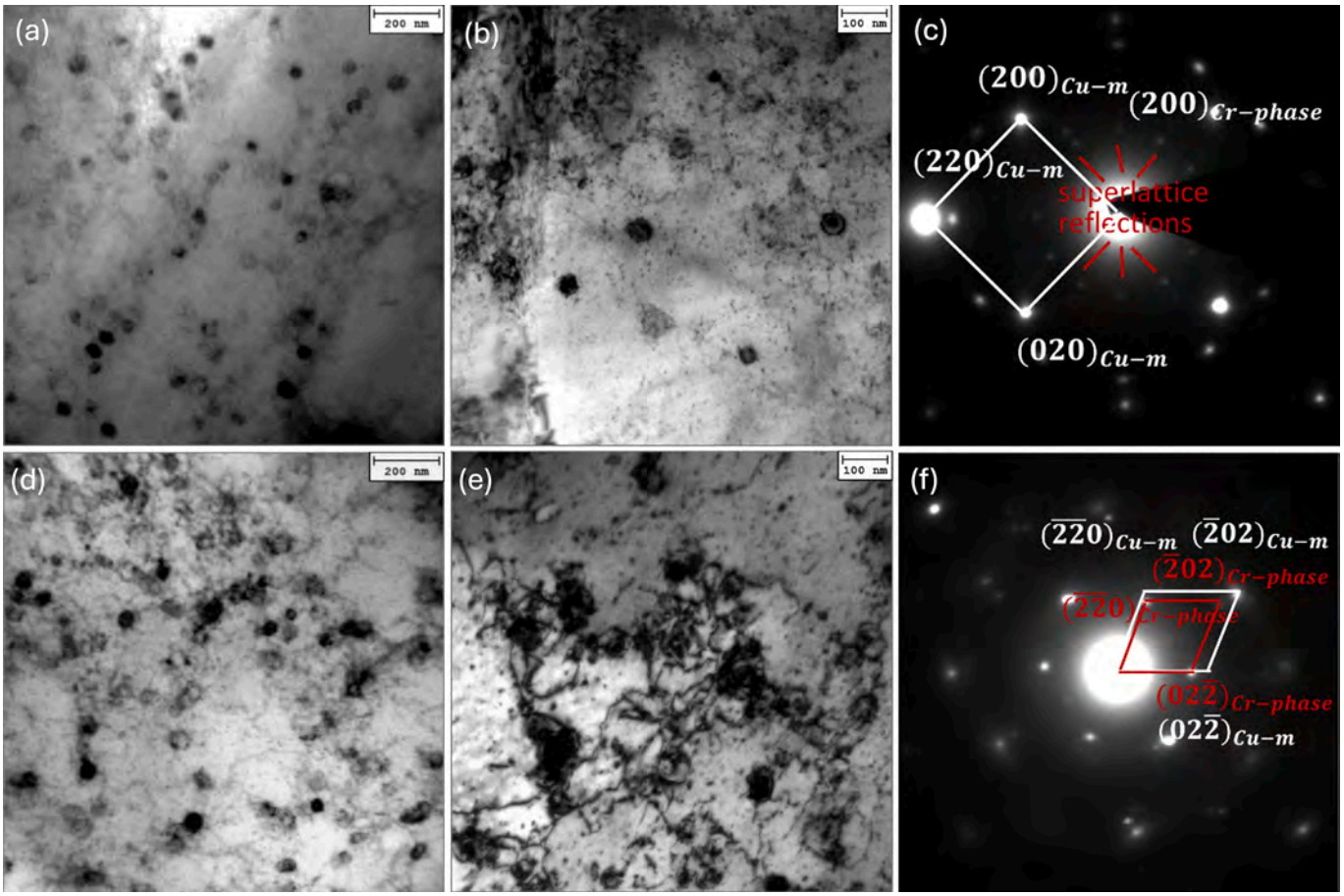

Fig. 8. a), b) Representative BF-TEM micrographs showing the detected nanometric particles observed in S2_2 at two different magnifications; c) indexed SAEDP recorded on one of the nanometric phase particles. The SAEDP in c) reports superlattice reflection spots that suggest a partial dissolution of the nanometric particle from which it was recorded. This feature was observed in several cases in the S2_2 sample; d), e) representative BF-TEM micrographs showing the detected nanometric particles observed in S2_3 at two different magnifications; f) indexed SAEDP recorded on one of the nanometric phase particles. The SAEDP in f) is a representative diffraction relationship between the Cu-matrix and the quasi-spherical Cr-rich phase particles.

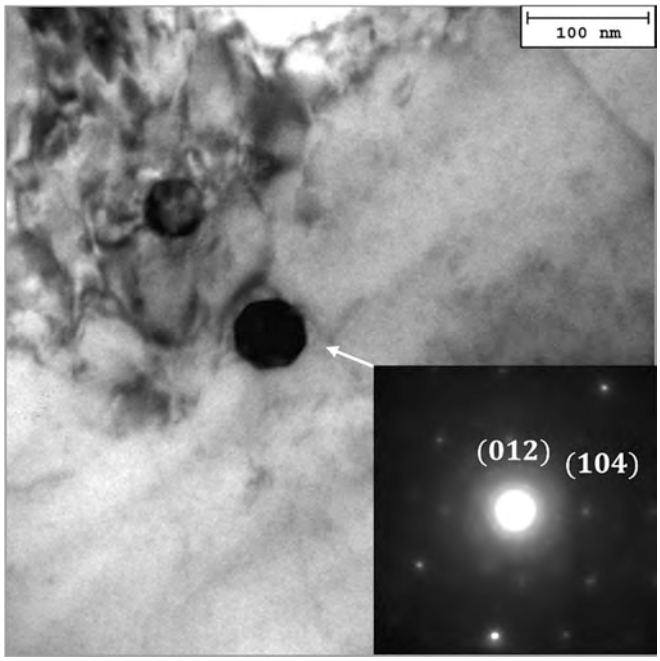

Fig. 9. Identification of the Cr_2O_3 *oxide phase by SAEDP (case of S2_3).*

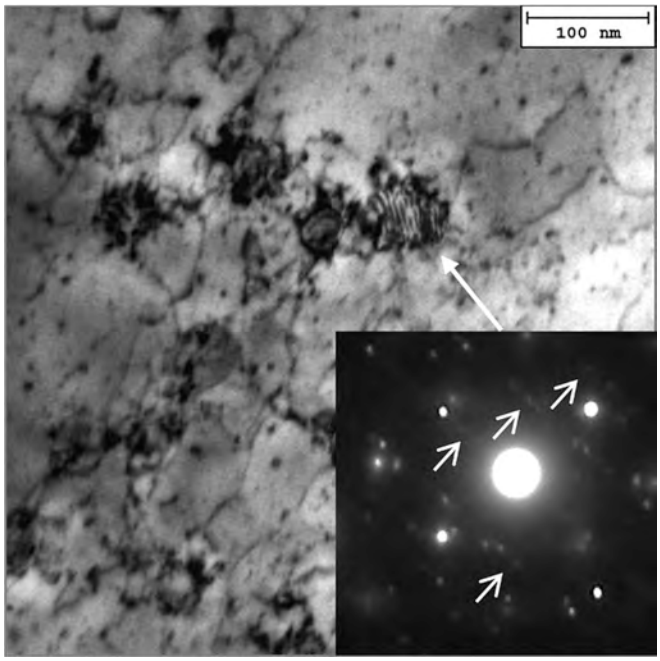

Fig. 10. GPZs observed in S2_2 sample.

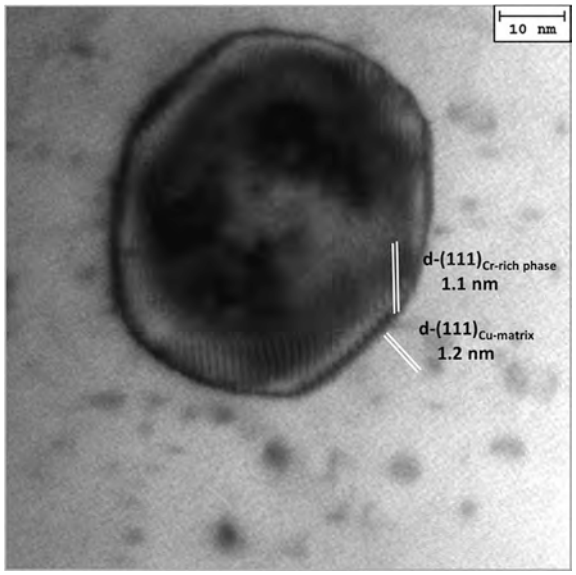

Fig. 11. Relationship existing along the crystallographic direction (111) for the nanometric Cr-rich phase and the surrounding Cu-matrix. The particle is dissolving under the action of the beam and the outskirt of the particle starts to show its atomic plane orientation. The plane distance was measured by an image analysis software (Leica Image pro-plus®) by further magnifying the present micrograph.

phase particles (Fig. 5(c)) SAEDP patterns are likely to complies with Cu_xZr_y with possible variants of Cu_4Zr or Cu_5Zr, but also Cu_8Zr_3, $Cu_{10}Zr_7$, and $Cu_{51}Zr_{14}$. Anyhow, in the present case, and based on the here performed analyses, it was not possible to determine with sufficient confidence the exact stoichiometric nature of such nanometric phase particles.

A statistical evaluation of the mean size and size distribution of the detected quasi-spherical particles was carried out for both S2_2 and S2_3 conditions, with the results presented in Fig. 12. The particle mean size, d_V, was found to be approximately 50 nm in both the cases. Correspondingly, the particle size distribution showed only little variation between the two experimental conditions. On the other hand, the particle volume fraction, f_V, drastically differed, as it resulted to be f_V = 1.7%, in the S2_2 experimental condition, and some 30 % higher in the S2_3 condition, accounting to f_V = 2.2%.

In this respect, it could be argued that the higher VED used in the S2_2 experimental condition, is likely to be responsible for a Cr-rich nanometric particle dissolution process, that yield to a local redistribution of Cr and Zr atoms from a fraction of these Cr-rich and Zr-containing nanometric precipitates.

Since the mean particle size only slightly changed and the dimensional distribution between S2_2 and S2_3 showed only a minor shift towards smaller sizes, the observed differences seem to converge to a massive energy-induced particle dissolution process. This phenomenon proceeds to fully dissolve some of the nanometric phases, causing Cr and Zr atoms to spread in the first vicinity of the dissolved particle sites rather than a gradual redistribution of atoms.

The quasi-spherical Cr-rich particles, significantly strengthen the CuCrZr alloy. In a considerably number of cases, the precipitation appeared at the sub-grains and grain boundaries. Thence, the high local strain energy concentrated in these locations facilitates the diffusion of Cr atoms, to promote the precipitation. Furthermore, as reported in Fig. 8(d-e) and in Fig. 13, the S2_3 condition exhibited a considerably large fraction of tangled dislocations in the vicinity and surrounding regions of the spherical Cr-rich aggregates.

That is, the Cr-rich nanometric phase particles accounting for a strengthening contribution to the alloy through a typical Orowan mechanism [41]. This was observed to be more significant in the in S2_3, compared to the case of the S2_2 experimental condition.

3.4. Vickers microhardness

The Vickers microhardness of the analysed samples is presented in Table 4. The hardness values achieved by the samples are in line with those reported in literature studies on direct aged samples [35,42,43]. Moreover, it is interesting to notice that both the conditions are in line

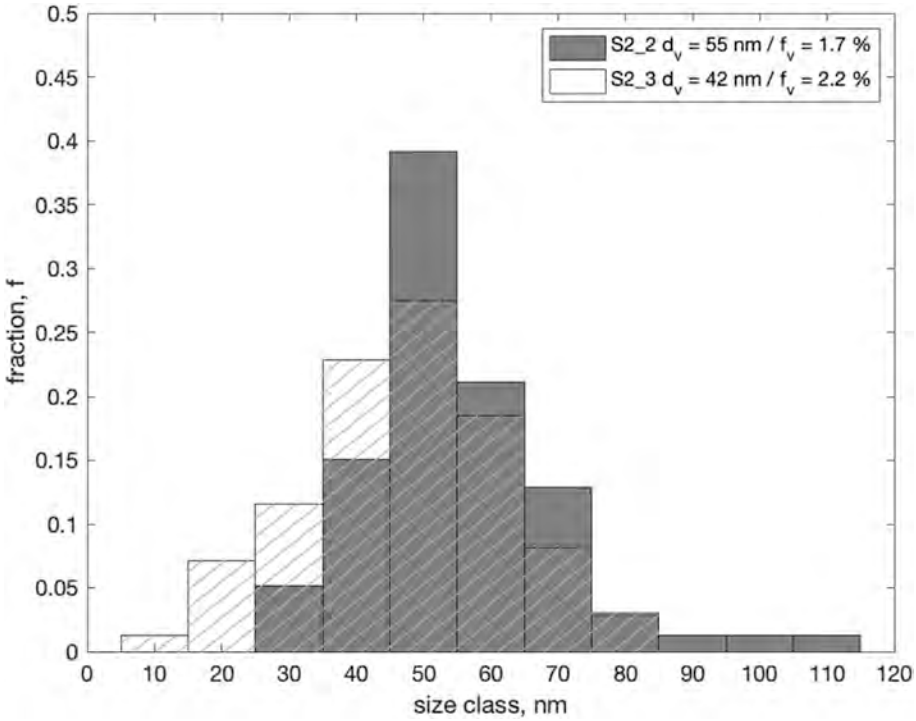

Fig. 12. Statistical evaluation of the size distribution, mean size and volume fraction of the Cr-rich quasi-spherical particles detected in S2_2 and S2_3.

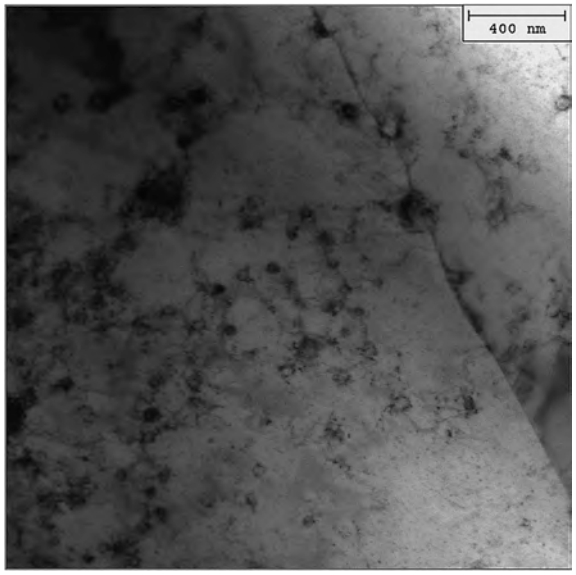

Fig. 13. Nanometric Cr-rich particles surrounded by tangled dislocations and located at sub-grain boundaries in S2_3.

Table 4
Vickers microhardness in the optimal process windows and YS values calculated using Eq. (6).

	S2_2	S2_3
HV1	118 ± 17	139 ± 15
YS [MPa] (calculated)	339	399

with the value of 128 HV reported as benchmark by ITER for a CuCrZr component after solution annealing and aging.

Krishna et al. [44] demonstrate a strong linear correlation between yield strength (YS) and Vickers microhardness (HV) for many copper alloys, including the one under investigation. They found a linear model that aligns accurately with experimental data across a wide range of measurements (from 50 to 1200 MPa) as follows:

$$YS = 2.874{*}HV \tag{6}$$

Moreover, the relationship of Eq. (6) suggested the possibility to investigate the different strengthening contributions, that according to many literature studies can be modelled to the yield strength (YS), converting them into hardness. The idea behind this approach is to give a better understanding of the microstructural evolution highlighting which are the main strengthening contributions among the multiple phenomena occurring in processing in a qualitative way.

For this alloy the YS can be assumed as the sum of the following contributions [45]:

$$YS = \sigma_0 + \Delta\sigma_{GS} + \Delta\sigma_{SS} + \Delta\sigma_{DS} + \Delta\sigma_{PS} \tag{7}$$

where σ_0 represents the initial frictional stress or Peierls-Nabarro stress, which can be assumed to be 20 MPa for copper [46–48]. The term $\Delta\sigma_{GS}$ denotes the contribution from grain size, $\Delta\sigma_{SS}$ represents the contribution from solid solution strengthening, $\Delta\sigma_{DS}$ accounts for dislocation strengthening, and $\Delta\sigma_{PS}$ pertains to the precipitation strengthening according to the Orowan model.

To investigate the impact of process parameters and to gain a deeper understanding of the strengthening mechanisms in this material, each contribution has been individually examined under optimized conditions.

The grain size contribution follows the Hall-Petch relation that can be described by the equation [47]:

$$\Delta\sigma_{GS} = \frac{k}{\sqrt{D}}; \tag{8}$$

where D represents the average grain size; due to the presence of columnar grains, the considered size was calculated by considering the section orthogonal to the building direction for a conservative approach (Table 3, Section 3.2). A similar assumption has been made by Salvan et al. [10]. k is the Hall Petch slope assumed to be 180 MPa•$\mu^{1/2}$ [45,48].

The dislocation strengthening mechanism accounts for the phenomenon where the presence of numerous intersecting dislocations in a crystal lattice impedes the movement of additional dislocations. This effect can be quantified with the following relation [49]:

$$\Delta_{DS} = \alpha MGb\sqrt{\rho_o} \tag{9}$$

where α is a constant assumed to be 0,23 for copper [46], M the Taylor factor, equal to 3,06 [46,49], G the shear modulus of the matrix of 45,5 GPa [10,45,50], b the burger vector of 0,256 nm [9,51], and finally ρ_o represents the dislocation density assessed through the KAM analysis (as described in Section 2.3, Eq. (1)). This contribution, that in the investigated samples can be considered as the primary strengthening contribution, relying them on the *as-built* condition, is notably influenced by the thermal history. It is widely acknowledged that it primarily stems from the high cooling rate which characterize local solidification of the additive processes, which prompts the dislocations formation [10].

The precipitation strengthening of this material, instead, as amply discussed in the previous section is attributed to the Orowan-Ashby model which attains the equation [48]:

$$\Delta\sigma_{PS} = \frac{0,8MGb}{2\pi\sqrt{1-\nu}} \frac{ln\left(\frac{2r}{b}\right)}{\lambda - 2r} \tag{10}$$

where r is the average radius of the precipitates measured from the bright-field TEM images,ν the Poisson's ratio equal to 0,34 [45], λ is the average crystal plane spacing between precipitates calculated from the following equation as a function of the volumetric fraction of precipitates f_V (Section 2.3, Eq. (4)) [48,52]:

$$\lambda = r\left(\sqrt{\frac{2\pi}{3f_V}} - 1,63\right) \tag{11}$$

Concerning the solid solution strengthening, finally, this contribution accounts for the crystal lattice distortion, which hinders dislocation motion. The contribution can be described as [9]:

$$\Delta\sigma_{SS} = MG\varepsilon^{\frac{3}{2}}\sqrt{\frac{x_a}{3}} \tag{12}$$

where ε, assumed as 0,25 [53,54], pertains to the misfit strain caused by lattice distortion around the solute elements, and x_a relates to the mass fraction of the alloying elements in the matrix. Although both Cr and Zr are fully soluble in copper, the contribution from Zr is negligible due to its extremely limited amount as an alloying element. Regarding Cr, even if all the atoms were in solid solution, x_a would be 0.84 % (Table 1). However, the nearly flat spectra observed in DSC measurements (Fig. 6) and the previous considerations suggests almost complete precipitation, allowing this contribution to be neglected.

The objective of the previously discussed calculations is summarized

Table 5
Numerical estimation of the strengthening contributions for CuCrZr in the two processing conditions.

	$\Delta\sigma_{GS}$ [MPa]	$\Delta\sigma_{SS}$ [MPa]	$\Delta\sigma_{DS}$ [MPa]	$\Delta\sigma_{PS}$ [MPa]
S2_2	11	–	158	49
S2_3	25	–	120	95

in Table 5.

Based on these results, the estimated numerical yield strength can be assumed to be 237 MPa and 259 MPa for the samples S2_2 and S2_3 respectively, which can be related thanks to the Eq. (6) to a hardness of $\approx 82HV$ and $\approx 90HV$ as reported in Fig. 14. The numerical model thence underestimates the real values of the 25 %; going back to literature the model tends to involve in underestimation when applied on samples in *as-built* condition [9,10]. This discrepancy can be related to many factors such as the difficulty in estimating the finer precipitation fraction from TEM imaging and also from the mathematical model correlating the hardness to the strength itself. It is anyway able to fit the experimental hardness difference for the two conditions. As already predictable the main strengthening factor comes from the intricate dislocation network coming from the process. Given that the EB-PBF process is conducted under high vacuum conditions, the physics governing heat transfer predominantly involves conduction, as radiation losses are limited due to the small dimension of the area involved in the melting. Conduction heat transfer adheres to Fourier's law, thereby being directly proportional to the thermal gradient. Consequently, employing a lower scanning speed increases the penetration of the molten pool, hence the heat transfer and subsequently improves the degree of undercooling. This could explain the difference registered in the two presented conditions.

4. Conclusions

In this study, the microstructural evolution and precipitation behaviour of CuCrZr in the EB-PBF process were thoroughly investigated under various process conditions. The process achieves high-density components (99.8 %) with good comprehensive properties. The main conclusions are as follows:

- The directional solidification inherent to the process, combined with the material intrinsic heat conduction properties, results in the formation of columnar grains that are highly textured along the building direction in both (100) and (111) orientations. Grain size is strongly influenced by processing conditions, with recrystallization phenomena leading to grain sizes ranging from 50 to 275 μm.
- The thermal evolution during the process facilitates the almost complete precipitation of alloying elements, typically achieved through well-defined post process thermal treatments, already in the *as-built* condition. This results in quasi-spherical Cr-rich and Zr-rich particles forming by an in-situ aging process. However, some diamond-like Cr_2O_3 precipitates are observed, likely due to the high susceptibility of Cr to oxidation, even under vacuum conditions. The relationship between the copper matrix and Cr-rich spherical secondary phases aligns with (110) Cr-rich || (111) Cu-matrix and (100) Cr-rich || (110) Cu-matrix orientations. While precipitate size is not directly related to the process conditions, the energetic input significantly affects the volumetric fraction and distribution of these particles.
- The material hardness in optimal processing conditions is 140 HV, corresponding to a numerically calculated yield strength of approximately 400 MPa. The primary strengthening mechanism is dislocation strengthening, resulting from the rapid local cooling rate in the molten pool. Additionally, the energetic input plays a crucial role in Orowan strengthening due to the energy-induced dissolution of secondary phases.

Based on these findings, it can be stated that the EB-PBF process is a viable method for applications requiring high thermal flux, which are typically addressed by this material. The thermal evolution associated with an in situ thermal treatment drastically changes the material microstructure compared to conventional manufacturing and laser-based additive techniques. This highlights the inefficacy of the conventional heat treatments (SAHT and DAHT) recommended for this material. The detected secondary phases are extremely temperature-stable, making their dissolution in solutioning a challenging task. Conversely, the intricate dislocation network created by the process seems to compensate for the inevitable growth of precipitates. Despite their size, these precipitates provide good initial thermal stability, enabling the material to withstand the usual cyclic thermal loads of such applications. Moreover, the demonstrated energy dissolution process opens the possibility of tuning the process parameters to limit the coarsening effect suggesting the potential to adjust the process to eliminate the need for postprocessing. However, further in-depth mechanical characterization is recommended to validate the model more accurately, considering the size effect on the resultant component.

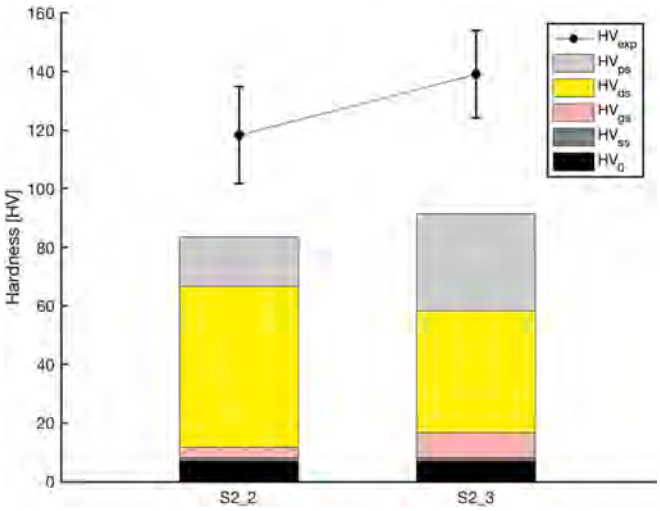

Fig. 14. Experimental hardness in comparison to the numerical model.

CRediT authorship contribution statement

Stefano Felicioni: Writing – original draft, Methodology, Investigation. **Elisa Padovano:** Writing – review & editing, Visualization, Validation, Investigation. **Federica Bondioli:** Writing – review & editing, Methodology, Funding acquisition, Formal analysis, Conceptualization. **Paolo Fino:** Project administration, Funding acquisition.

Declaration of competing interest

The authors declare that there is no conflict of interest regarding the publication of this paper. No financial or personal relationships exist with other people or organizations that could inappropriately influence this work.

Data availability

Data will be made available on request.

Acknowledgments

This research did not receive any specific grant from funding agencies in the public, commercial, or not-for-profit sectors.

References

[1] W.M. Haynes, CRC Handbook of Chemistry and Physics, 2017.
[2] R.P. Minneci, E.A. Lass, J.R. Bunn, H. Choo, C.J. Rawn, Copper-based alloys for structural high-heat-flux applications: a review of development, properties, and performance of Cu-rich Cu–Cr–Nb alloys, Int. Mater. Rev. 66 (6) (2021) 394–425, https://doi.org/10.1080/09506608.2020.1821485.
[3] A.H. Seltzman, S.J. Wukitch, Nuclear response of additive manufactured GRCop-84 copper for use in lower hybrid launchers in a fusion environment, Fusion Eng. Des. 159 (2020) 111726, https://doi.org/10.1016/j.fusengdes.2020.111726.

[4] G.E. Dieter, D.J. Bacon, Mechanical metallurgy, in: SI metric (Ed.), McGraw-Hill Series in Materials Science and Engineering, McGraw-Hill, London, 1988.

[5] F. Canillas, et al., On the feasibility to obtain CuCrZr alloys with outstanding thermal and mechanical properties by additive manufacturing, J. Nucl. Mater. 601 (2024) 155304, https://doi.org/10.1016/j.jnucmat.2024.155304.

[6] F. Singer, D.C. Deisenroth, D.M. Hymas, M.M. Ohadi, Additively manufactured copper components and composite structures for thermal management applications, in: 2017 16th IEEE Intersociety Conference on Thermal and Thermomechanical Phenomena in Electronic Systems (ITherm), 2017, pp. 174–183, https://doi.org/10.1109/ITHERM.2017.7992469.

[7] D.A. Porter, K.E. Easterling, M.Y. Sherif, Phase Transformations in Metals and Alloys, Fourth edition, CRC Press, Taylor & Francis Group, Boca Raton, 2022.

[8] X. Tang, et al., A study on the mechanical and electrical properties of high-strength CuCrZr alloy fabricated using laser powder bed fusion, J. Alloys Compd. 924 (2022) 166627, https://doi.org/10.1016/j.jallcom.2022.166627.

[9] X. Yang, Y. Qi, W. Zhang, Y. Wang, H. Zhu, Laser powder bed fusion of C18150 copper alloy with excellent comprehensive properties, Mater. Sci. Eng. A 862 (2023) 144512, https://doi.org/10.1016/j.msea.2022.144512.

[10] C. Salvan, L. Briottet, T. Baffie, L. Guetaz, C. Flament, CuCrZr alloy produced by laser powder bed fusion: microstructure, nanoscale strengthening mechanisms, electrical and mechanical properties, Mater. Sci. Eng. A 826 (2021) 141915, https://doi.org/10.1016/j.msea.2021.141915.

[11] D.A. Ramirez, et al., Novel precipitate–microstructural architecture developed in the fabrication of solid copper components by additive manufacturing using electron beam melting, Acta Mater. 59 (10) (2011) 4088–4099, https://doi.org/10.1016/j.actamat.2011.03.033.

[12] R. Guschlbauer, A.K. Burkhardt, Z. Fu, C. Körner, Effect of the oxygen content of pure copper powder on selective electron beam melting, Mater. Sci. Eng. A 779 (2020) 139106, https://doi.org/10.1016/j.msea.2020.139106.

[13] T. Wolf, Z. Fu, C. Körner, Selective electron beam melting of an aluminum bronze: microstructure and mechanical properties, Mater. Lett. 238 (2019) 241–244, https://doi.org/10.1016/j.matlet.2018.12.015.

[14] N. Ordás, et al., Development of CuCrZr via electron beam powder bed fusion (EB-PBF), J. Nucl. Mater. 548 (2021) 152841, https://doi.org/10.1016/j.jnucmat.2021.152841.

[15] European Committee For Standardization, Metallic Products - Types of Inspection Documents, 2004.

[16] R. Guschlbauer, S. Momeni, F. Osmanlic, C. Körner, Process development of 99.95% pure copper processed via selective electron beam melting and its mechanical and physical properties, Mater. Charact. 143 (2018) 163–170, https://doi.org/10.1016/j.matchar.2018.04.009.

[17] A.P. Zhilyaev, I. Shakhova, A. Morozova, A. Belyakov, R. Kaibyshev, Grain refinement kinetics and strengthening mechanisms in Cu–0.3Cr–0.5Zr alloy subjected to intense plastic deformation, Mater. Sci. Eng. A 654 (2016) 131–142, https://doi.org/10.1016/j.msea.2015.12.038.

[18] U. Holzwarth, H. Stamm, The precipitation behaviour of ITER-grade Cu–Cr–Zr alloy after simulating the thermal cycle of hot isostatic pressing, J. Nucl. Mater. 279 (1) (2000) 31–45, https://doi.org/10.1016/S0022-3115(99)00285-8.

[19] E04 Committee, Test Methods for Determining Average Grain Size, 2021, https://doi.org/10.1520/E0112-13R21.

[20] E04 Committee, Test Method for Microindentation Hardness of Materials, ASTM International, 2022, https://doi.org/10.1520/E0384-22.

[21] E. Sharabian, M. Leary, D. Fraser, S. Gulizia, Electron beam powder bed fusion of copper components: a review of mechanical properties and research opportunities, Int. J. Adv. Manuf. Technol. 122 (2) (2022) 513–532, https://doi.org/10.1007/s00170-022-09922-6.

[22] A. Thomas, G. Fribourg, J.-J. Blandin, P. Lhuissier, R. Dendievel, G. Martin, Tailoring the crystallographic texture of pure copper through control of the scanning strategy in electron powder bed fusion, Materialia 24 (2022) 101495, https://doi.org/10.1016/j.mtla.2022.101495.

[23] D. Bourell, et al., Materials for additive manufacturing, CIRP Ann. 66 (2) (2017) 659–681, https://doi.org/10.1016/j.cirp.2017.05.009.

[24] M. Shao, S. Vijayan, P. Nandwana, J.R. Jinschek, The effect of beam scan strategies on microstructural variations in Ti-6Al-4V fabricated by electron beam powder bed fusion, Mater. Des. 196 (2020) 109165, https://doi.org/10.1016/j.matdes.2020.109165.

[25] H.E. Helmer, C. Körner, R.F. Singer, Additive manufacturing of nickel-based superalloy Inconel 718 by selective electron beam melting: processing window and microstructure, J. Mater. Res. 29 (17) (2014) 1987–1996, https://doi.org/10.1557/jmr.2014.192.

[26] A. Rai, H. Helmer, C. Körner, Simulation of grain structure evolution during powder bed based additive manufacturing, Addit. Manuf. 13 (2017) 124–134, https://doi.org/10.1016/j.addma.2016.10.007.

[27] Y.S. Lee, et al., Role of scan strategies on thermal gradient and solidification rate in electron beam powder bed fusion, Addit. Manuf. 22 (2018) 516–527, https://doi.org/10.1016/j.addma.2018.04.038.

[28] M. Gäumann, S. Henry, F. Cléton, J.-D. Wagnière, W. Kurz, Epitaxial laser metal forming: analysis of microstructure formation, Mater. Sci. Eng. A 271 (1–2) (1999) 232–241, https://doi.org/10.1016/S0921-5093(99)00202-6.

[29] G. Durashevich, V. Cvetkovski, V. Jovanovich, Effect of thermomechanical treatment on mechanical properties and electrical conductivity of a CuCrZr alloy, Bull. Mater. Sci. 25 (1) (2002) 59–62, https://doi.org/10.1007/BF02704596.

[30] A. Vinogradov, V. Patlan, Y. Suzuki, K. Kitagawa, V.I. Kopylov, Structure and properties of ultra-fine grain Cu–Cr–Zr alloy produced by equal-channel angular pressing, Acta Mater. 50 (7) (2002) 1639–1651, https://doi.org/10.1016/S1359-6454(01)00437-2.

[31] R. Kočiško, et al., The mechanical properties of OFHC copper and CuCrZr alloys after asymmetric rolling at ambient and cryogenic temperatures, Open Eng. 8 (1) (2018) 426–431, https://doi.org/10.1515/eng-2018-0041.

[32] B.N. Singh, D.J. Edwards, M. Eldrup, P. Toft, Effects of heat treatments and neutron irradiation on microstructures and physical and mechanical properties of copper alloys, J. Nucl. Mater. 249 (1) (1997) 1–16, https://doi.org/10.1016/S0022-3115(97)00184-0.

[33] G. Piatti, D. Boerman, Hot tensile characteristics and microstructure of a Cu-0.65Cr-0.08Zr alloy for fusion reactor applications, J. Nucl. Mater. 185 (1) (1991) 29–38, https://doi.org/10.1016/0022-3115(91)90362-B.

[34] M. Appello, P. Fenici, Solution heat treatment of a Cu Cr Zr alloy, Mater. Sci. Eng. A 102 (1) (1988) 69–75, https://doi.org/10.1016/0025-5416(88)90534-4.

[35] S. Zhang, H. Zhu, L. Zhang, W. Zhang, H. Yang, X. Zeng, Microstructure and properties of high strength and high conductivity Cu-Cr alloy components fabricated by high power selective laser melting, Mater. Lett. 237 (2019) 306–309, https://doi.org/10.1016/j.matlet.2018.11.118.

[36] J. Liu, et al., In-situ TEM study of the dynamic interactions between dislocations and precipitates in a Cu-Cr-Zr alloy, J. Alloys Compd. 765 (2018) 560–568, https://doi.org/10.1016/j.jallcom.2018.06.158.

[37] G. Ma, et al., Microstructure evaluation and resultant mechanical properties of laser- arc hybrid additive manufactured Cu-Cr-Zr alloy, J. Alloys Compd. 912 (2022) 165044, https://doi.org/10.1016/j.jallcom.2022.165044.

[38] A. Morozova, R. Mishnev, A. Belyakov, R. Kaibyshev, Microstructure and properties of fine grained Cu-Cr-Zr alloys after termo-mechanical treatments, Rev. Adv. Mater. Sci. 54 (1) (2018) 56–92, https://doi.org/10.1515/rams-2018-0020.

[39] T. Fujii, H. Nakazawa, M. Kato, U. Dahmen, Crystallography and morphology of nanosized Cr particles in a Cu–0.2% Cr alloy, Acta Mater. 48 (5) (2000) 1033–1045, https://doi.org/10.1016/S1359-6454(99)00411-5.

[40] X. Tang, X. Chen, F. Sun, P. Liu, H. Zhou, S. Fu, The current state of CuCrZr and CuCrNb alloys manufactured by additive manufacturing: a review, Mater. Des. 224 (2022) 111419, https://doi.org/10.1016/j.matdes.2022.111419.

[41] L. Peng, et al., The phase transformation and strengthening of a Cu-0.71 wt% Cr alloy, J. Alloys Compd. 708 (2017) 1096–1102, https://doi.org/10.1016/j.jallcom.2017.03.069.

[42] Y. Bai, C. Zhao, Y. Zhang, J. Chen, H. Wang, Additively manufactured CuCrZr alloy: microstructure, mechanical properties and machinability, Mater. Sci. Eng. A 819 (2021) 141528, https://doi.org/10.1016/j.msea.2021.141528.

[43] K. Jahns, R. Bappert, P. Böhlke, U. Krupp, Additive manufacturing of CuCr1Zr by development of a gas atomization and laser powder bed fusion routine, Int. J. Adv. Manuf. Technol. 107 (5–6) (2020) 2151–2161, https://doi.org/10.1007/s00170-020-04941-7.

[44] S.C. Krishna, N.K. Gangwar, A.K. Jha, B. Pant, On the prediction of strength from hardness for copper alloys, J. Mater. 2013 (2013) 1–6, https://doi.org/10.1155/2013/352578.

[45] Y. Liu, Z. Li, Y. Jiang, Y. Zhang, Z. Zhou, Q. Lei, The microstructure evolution and properties of a Cu–Cr–Ag alloy during thermal-mechanical treatment, J. Mater. Res. 32 (07) (2017) 1324–1332, https://doi.org/10.1557/jmr.2017.17.

[46] S. Zhang, H. Zhu, L. Zhang, W. Zhang, H. Yang, X. Zeng, Microstructure and properties in QCr0.8 alloy produced by selective laser melting with different heat treatment, J. Alloys Compd. 800 (2019) 286–293, https://doi.org/10.1016/j.jallcom.2019.06.018.

[47] N. Hansen, Hall–Petch relation and boundary strengthening, Scr. Mater. 51 (8) (2004) 801–806, https://doi.org/10.1016/j.scriptamat.2004.06.002.

[48] J. Chen, J. Wang, X. Xiao, H. Wang, H. Chen, B. Yang, Contribution of Zr to strength and grain refinement in Cu Cr Zr alloy, Mater. Sci. Eng. A 756 (2019) 464–473, https://doi.org/10.1016/j.msea.2019.04.053.

[49] S. Huang, W. Huang, W. Xie, H. Chen, H. Wang, B. Yang, Microstructure and strengthening mechanisms of CuCrZr alloy by two-step thermomechanical treatment, J. Mater. Sci. Mater. Electron. 31 (20) (2020) 17798–17809, https://doi.org/10.1007/s10854-020-04333-3.

[50] J. Zhou, et al., Microstructure and properties of powder metallurgy Cu-1%Cr-0.65%Zr alloy prepared by hot pressing, Vacuum 131 (2016) 156–163, https://doi.org/10.1016/j.vacuum.2016.06.008.

[51] Q. Lei, Z. Li, A. Zhu, W. Qiu, S. Liang, The transformation behavior of Cu–8.0Ni–1.8Si–0.6Sn–0.15Mg alloy during isothermal heat treatment, Mater. Charact. 62 (9) (2011) 904–911, https://doi.org/10.1016/j.matchar.2011.06.008.

[52] E. Orowan, Fracture and Strength of Solids, 1949.

[53] P. Guan, et al., Effect of selective laser melting process parameters and aging heat treatment on properties of CuCrZr alloy, Mater. Res. Express 6 (11) (2019), https://doi.org/10.1088/2053-1591/ab4e2f, 1165c1.

[54] H. Feng, H. Jiang, D. Yan, L. Rong, Effect of continuous extrusion on the microstructure and mechanical properties of a CuCrZr alloy, Mater. Sci. Eng. A 582 (2013) 219–224, https://doi.org/10.1016/j.msea.2013.06.031.